RSC Advances

Photonic Crystal-based CdS-Au-WO3 Heterostructure for Efficient Visible-Light Photocatalytic Hydrogen and Oxygen Evolution

Journal:	*RSC Advances*
Manuscript ID:	RA-COM-02-2014-001415.R1
Article Type:	Communication
Date Submitted by the Author:	11-Mar-2014
Complete List of Authors:	Cui, Xiaofeng; China Petroleum University, State Key Laboratory of Heavy Oil Wang, Yajun; China Petroleum University, State Key Laboratory of Heavy Oil Jiang, Guiyuan; China Petroleum University, State Key Laboratory of Heavy Oil Zhao, Zhen; China University of Petroleum, State Key Lab of Heavy Oil Xu, Chunming; State Key Laboratory of Heavy Oil Processing, Wei, Yuechang; China University of Petroleum, State Key Lab of Heavy Oil Duan, Aijun; China Petroleum University, State Key Laboratory of Heavy Oil Liu, Jian; China Petroleum University, State Key Laboratory of Heavy Oil Gao, Jinsen; China Petroleum University, Chemical Engineering

The table of contents entry

Photonic crystal-based CdS-Au-WO_3 heterostructure that integrates slow photon effect and superior electron transfer exhibits efficient photocatalytic H_2 and O_2 evolution.

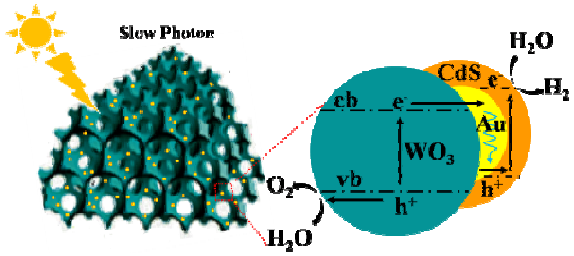

Cite this: DOI: 10.1039/c0xx00000x

www.rsc.org/xxxxxx

ARTICLE TYPE

Photonic Crystal-based CdS-Au-WO_3Heterostructure for Efficient Visible-Light Photocatalytic Hydrogen and Oxygen Evolution

Xiaofeng Cui,[#] Yajun Wang,[#] Guiyuan Jiang,* Zhen Zhao, Chunming Xu,* Yuechang Wei, Aijun Duan, Jian Liu, Jinsen Gao

Received (in XXX, XXX) Xth XXXXXXXXX 20XX, Accepted Xth XXXXXXXXX 20XX
DOI: 10.1039/b000000x

A photonic crystal-based CdS-Au-WO_3 heterostructure was constructed on the WO_3 photonic crystal segments. Highly efficient visible-light-driven hydrogen and oxygen evolution are demonstrated relative to those of single-, two-component and unstructured systems due to good light harvesting of photonic crystals and efficient electron transfer of this heterostructure.

Powdered semiconductor solar water splitting provides a sustainable proposal for large-scale H_2 production, and it has been attracting extensive research in recent years.[1]The design and development of efficient photocatalyst is a critical issue in photocatalytic water splitting, which involves light absorption, photogenerated charge transfer/separation, and the subsequent catalysis, etc. Over the past decade, many strategies have been developed to improve photocatalysis efficiency, including doping,[2] coupling plasmonresonance,[3] and regulating morphology, size and crystal facet of photocatalysts etc.[4] Among these tactics, constructing heterostructure has been demonstrated effective for improving photocatalytic efficiency through promoting the photogenerated charge separation and harvesting visible light. Various types of two-component semiconductor heterostructure have been reported, such as CdS/WO_3,[5] CdS/TiO_2,[6] C_3N_4/ZnO.[7] On this basis, recently study further demonstrated that introducing an electron transfer mediator, such as Au,[8] Ag[9] and graphene oxide[10] into the heterostructure interface can strengthen the interface charge transfer and result in a vectorial electron transfer, which can efficiently improve photogenerated separation and photocatalytic activity.

Because of owning a periodic dielectric contrast in the length scale of the wavelength of light, photonic crystals (PCs) offer a great capability of controlling and manipulating the flow of incident light, and they have been widely applying in optics and electronics in forms of optical switch,[11] photonic-crystal fibers[12] and optical transistors[13] etc. Recently, the unique optical performance of PCs for light harvesting via slow photon enhancement has been capturing growing interest in photocatalysis and photoelectrochemistry.[14] For example, TiO_2, WO_3 inverse opal PCs or PC segments were constructed and demonstrated enhanced performances for photodegradation methylene blue,[14a] photoelectrodes[14b,15] and hydrogen evolution[16]. However, most reported PCs are constructed on a single component, few cases have been reported on introducing a PC into heterostructure system to improve photocatalytic efficiency. Given the prominent advantage of PCs in light harvesting and the high efficiency of heterostructure in electron transfer, the construction of PC-based heterostructure for water splitting is expected to bring better properties and powerful platforms for photocatalytic applications.

Herein, we report for the first time a structural and visible-light responsive photonic crystal based heterostructure of CdS-Au-WO_3, which are assembled in a heterojunction array of CdS for reduction of water to H_2, the electron-transfer mediator of Au and WO_3 for oxidation of water to O_2. In the as-constructed system, the sub-components of CdS and WO_3 are both visible-light responsive, and WO_3 are structured into PC with promoted light absorbance via slow photon effect. On this basis, superior photocatalytic hydrogen and oxygen evolution on the as-prepared catalyst was demonstrated.

WO_3 inverse opal photonic crystals were prepared through a modified colloidal crystal template method.[17]Adjusting the size of template microspheres can vary the pore diameter of WO_3inverse opals continuously, and therefore, the stop-bands of WO_3 PCs are tunable by regulating the microsphere sizes. In order to get an appropriate stop-band position to improve the light harvesting efficiency through slow photon enhancement, three kinds of template spheres (diameter: 180, 240, and 310 nm) were selected to fabricate WO_3 PCs with their red-edge of the photonic stop-band potentially near its electronic absorption edge. (Fig.S1†)

Fig.1a-c presents SEM images of WO_3 inverse opal photonic crystals with different pore diameters which were fabricated from 180, 240 and 310 nm PMMA templates and denoted as WO_3-180, WO_3-240, and WO_3-310, respectively. It is indicated that the pores in the WO_3 inverse opal films are three-dimensionally highly ordered in a face-centered cubic (fcc) array and the voids are interconnected through open window. The average pore diameters of about 130±10, 175±10 and 230±10nm (determined by SEM image) were found to be 25%-35% shrinkage in comparison with the original PMMA microspheres due to polymer decomposition and precursor crystallization.[18] Fig.1d shows the reflectance spectra of as-prepared inverse opal PCs along the (111) plane after moistening by water (solid lines) and the absorbance spectrum of crushed WO_3 that obtained by crushing mixed PC segments of WO_3-180, WO_3-240 and WO_3-310, and denoted as WO_3-cru (dash line) (Fig.S2†). The inverse opals have stop bands maxima at 390, 430 and 525 nm,

respectively. The stop-band positions varied with the changing in the pore sizes, and red-shifted owing to larger pores packed with larger lattice constants.[19] These strong Bragg reflection peaks indicate that it formed high-quality inverse opal structure in a long range.

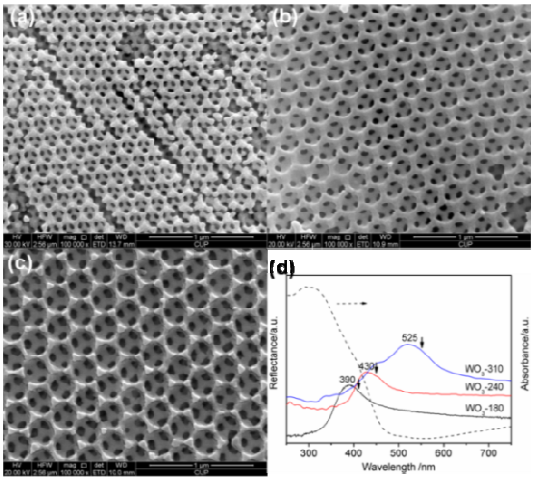

Fig.1SEM images of WO_3 inverse opal photonic crystals WO_3-180 (a), WO_3-240 (b), and WO_3-310 (c) fabricated from 180, 240 and 310 nm PMMA templates, respectively. Reflectance spectra of the photonic crystal films after moistening by water (solid lines) with stop bands maxima at 390, 430 and 525 nm and the red edge of stop band marked with arrows, and the absorbance spectrum of crushed WO_3 (dash line) (d).

To demonstrate the slow photon enhancement of the photonic-crystal structure on the photocatalytic activity of WO_3, photocatalytic water oxidation under visible light ($\lambda \geqq 420$ nm) was performed. A Xe lamp (300 W) with a 420 nm UV-cutoff filter was used as the visible-light source. The WO_3 inverse opal PCs with different pore diameters were exfoliated from the glass substrates and formed PC segments.The optical image shows the bright structural color of exfoliated segments under white light illumination, and the SEM image displays that the segments have highly ordered macrospores structure (Fig.S3†). These results demonstrate that the inverse opal photonic crystal structure still kept well in some range after exfoliating from the glass substrate. The BET testing indicates that the specific surface area of four samples are comparable (Table S1†). The PC segments were added to the aqueous solution with $AgNO_3$ as an electron capture reagent. Fig.2 shows the oxygen evolution time profiles of a series of WO_3 inverse opal PC segments and WO_3-cru. The three inverse opal samples display higher photocatalytic O_2 evolution activity than the crushed one, which may due to the slow photon enhancement and multiple scattering in the porous structure improving light harvesting. And the three inverse opal PC samples also show apparent difference in photocatalytic performances. The WO_3-240 exhibits the highest performance (18.2 $\mu mol \cdot h^{-1}$/20 mg), which is higher than the WO_3-180 (14.9 $\mu mol \cdot h^{-1}$/20 mg) and WO_3-310 (13.3 $\mu mol \cdot h^{-1}$/20 mg), and 1.5 times of the WO_3-cru(12.1 $\mu mol \cdot h^{-1}$/20 mg). The difference among them is the position of stop band resulting from different pore diameter. According to the reported results,[14a] the largest optical enhancement of slow photons is attained at the red edge of the stop band, approximately 20 nm (0.15 eV) away from the stop-band maximum. However, under white-light irradiation, the competition between slow photon enhancement and the suppressing of stop-band reflectivity on photoactivity must be considered carefully. In the case of WO_3-180, the stop band and red edge (ca. 410 nm) are within the WO_3 absorption region, and both stop-band reflection and slow photon enhancement are eliminated by the high absorbance. The intensity of slow photon effect is weakened.[14a] As for WO_3-240, the stop band maximum is located in the WO_3 absorption region and the slow photon wavelength (ca. 450 nm) overlapped with the electronic absorption edge of WO_3, so the stop band reflectivity is suppressed by the larger absorbance to some extent, and slow photon enhancement dominates. Furthermore, the intensity of light source is also a factor that needs to be considered. The light intensity at 450 nm is slightly stronger than that at 410 nm (Fig.S4†). So, more slow photons should be involved in the interaction between the photons and dielectric material for WO_3-240, and the oxygen evolution efficiency of WO_3-240 is higher than that of WO_3-180. For WO_3-310, the stop band and red edge (ca. 545 nm) are located out of the electronic absorption of WO_3, so the effects of stop-band reflection and slow photon enhancement not function for light harvesting. Although the light intensity at 545 nm is slightly stronger than that at 410 nm and 450 nm, the oxygen evolution efficiency is lowest among these PC samples. Therefore, the higher activity of WO_3-240 than those of other PC samples can be attributed to the appropriate stop-band position presenting a more intense slow photon enhancement which results in an increased light absorption as well as the enhanced light utilization.

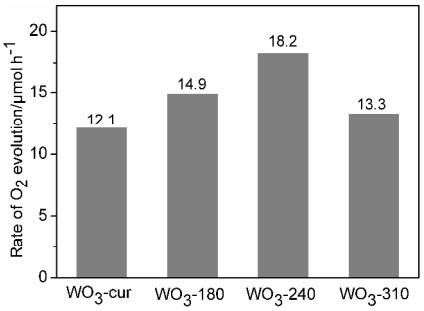

Fig.2 O_2 evolution profiles of WO_3-180,WO_3-240, and WO_3-310 photonic crystal segments and WO_3-cru under visible-light illumination over 100 mL aqueous solution containing 20 mg photocatalysts and 5 mmol $AgNO_3$ as sacrificial reagent; 300 W Xe arc lamp with a UV-cutoff filter (≥420 nm) used as the visible-light source.

For photocatalytic hydrogen evolution, the three components (3C) of CdS-Au-WO_3 Z-scheme system was constructed base on the optimized WO_3-240 PC segments. Firstly, Au nanoparticles were supported onto the framework of WO_3-240 PC segments via gas-bubbling-assisted membrane reduction method.[20] Fig.3 shows TEM and HRTEM images, as well as the size distribution of Au nanoparticles of Au-WO_3 which supported Au particles on the WO_3-240 PC segments. The three-dimensional ordered macroporous (3DOM) structure of Au-WO_3 PC segment can be clearly observed by TEM image (Fig.3a) after loading Au nanoparticles. The selected area electron diffraction (SAED) (inset in Fig.3a) demonstrates that the walls of the macroporous samples are highly crystalline, and clear diffraction spots shows that the skeleton of macropores is a big single crystallite of WO_3 rather than stacking by small crystalline grains like other metal oxide-based. It is consistent with the Ueda's results.[18] So that, the

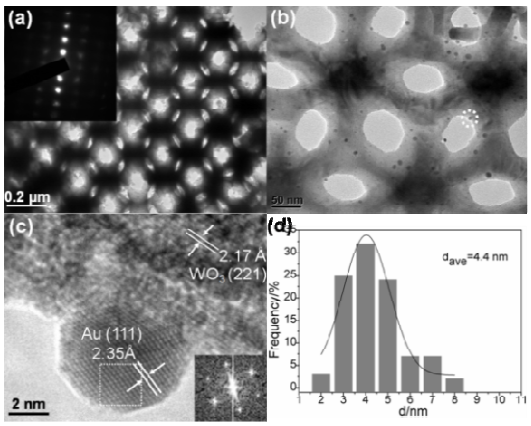

Fig.3 TEM images (a) (b), HRTEM image (c) and size distribution of Au nanoparticles (d) of Au-WO_3 after supporting Au particles on the WO_3-240 PC segments. The insets in (a) and (c) are the corresponding SAED pattern of WO_3 and FFT image of Au nanoparticle. The marked lattice and fringes in HRTEM image (c) correspond to the Au (111) plane at 2.35 Å and WO_3 (221) plane at 2.17 Å

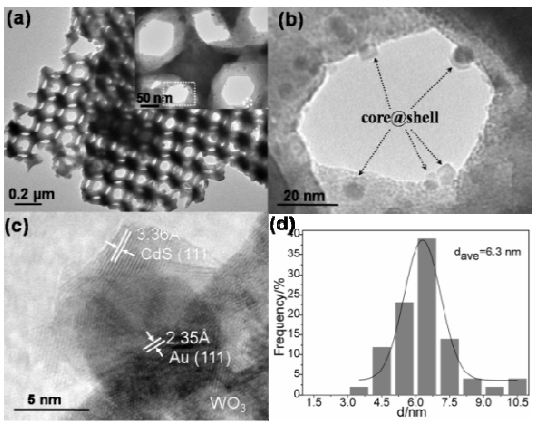

Fig.4 TEM images (a) (b), HRTEM image (c) and size distribution of Au-CdS nanoparticles (d) of CdS-Au-WO_3 after coating CdS on Au nanoparticles.The marked lattice and fringes in HRTEM image (c) correspond to the Au (111) plane at 2.35 Å and CdS (111) plane at 3.36 Å.

3DOM structure of WO_3 can be expected to more sturdily. After further enlarging the TEM image, Au nanoparticles decorated on the framework of 3DOM WO_3 support are displayed clearly in the Fig.3b, and it shows that the Au particles are highly dispersed and uniform in size. The two different planar spaces in HRTEM image (Fig.3c) were measured to be 2.35Å and 2.17 Å, which well match the (111) plane of gold nanoparticle and (221) plane of WO_3, respectively. The fast Fourier transform (FFT) image of Au particle (Figure 3c inset) indicates that the hemispherical gold particles located on the surface of WO_3 are crystalline with fcc (111) plane exposed. These results indicate that the in-situ growth mode of Au nanoparticles presents a tight contact between the WO_3 and Au particle, which provides a good basis for efficient electron transfer and subsequent coating of CdS. The size distribution pattern (Fig.3d) illustrates that the Au particle size is in the range of 2–8 nm with a narrow distribution and a mean diameter of 4.4 nm by statistic analysis of 100 Au particles.

Selective coating of CdS onto the Au particle is critical for the efficient electron transfer and for the successful construction of the solid state Z-scheme. Herein, a facile hydrothermal coprecipitation method was employed. Thioacetamide (TAA), a sulfur precursor, was firstly added into Au-WO_3 suspension solution and continuously stirred for 12 h so as to allow TAA absorb sufficiently onto the surface of Au particles by strong affinity of sulphur or -NH_2 for Au. Then the $Cd(NO_3)_2$ was added, and temperature programming (1°C/min) was performed. During the process, S^{2-} was released slowly from TAA onto the surface of Au particles, and crystalline CdS was thus *in-situ* formed through hydrothermal crystallization.[21] Fig.4 shows the TEM, HRTEM images and size distribution pattern of the CdS-Au nanoparticles of CdS-Au-WO_3 after coating CdS on Au nanoparticles. The TEM image (Fig.4a) shows that the 3DOM structure keeps well and particles (Fig.4a inset) supported on the framework of macrospores are still highly dispersed and uniform in size. The area magnification TEM image (Fig.4b) shows that the surface of Au nanoparticles coated with some materials and the particles displayed as a core-shell structure. The HRTEM image (Fig.4c) clearly shows two different lattice fringes on the core and shell, and the marked lattice fringes of 3.36 Å on the shell and 2.35Å on the core are indexed as (111) planes of CdS and Au nanoparticle, respectively. To investigate whether Au nanoparticles were coated universally, the XPS measurement was performed. According to the comparison of the XPS spectrum of CdS-Au-$WO_3$with that ofAu-WO_3, the intensity of Au signals is significantly weakened after coating of CdS (Fig. S5†), indicating that Au nanoparticles were covered universally. The very weak Au signals of CdS-Au-WO_3 may be attributed to small portion of X-ray penetrates the thin shell of CdS. The component and nanostructure of Au core and CdS shell were further confirmed by and energy-dispersive X-ray spectroscopy (EDS) (Fig. S6†). These results demonstrated that the CdS was coated selectively on the surface of Au particles and a CdS-Au-WO_3 heterostructure system was constructed successfully. The selective deposition and high-quality coating ensures the efficient photogenerated electron transfer and the subsequent photocatalysis. The size distribution pattern of coated nanoparticles (Fig.4d) illustrates that the particle size is in the range of 3-11 nm with a narrow distribution and a mean diameter of 6.3 nm by statistic analysis of 100 particles. Compared with the uncoated Au nanoparticles, the mean diameter of coated particle is increased by ca. 2 nm. Therefore, the thickness of coated CdS shell is about 2 nm, which is consistent with the HRTEM result.

Fig.5a presents the XRD patterns of WO_3-240, Au-WO_3, CdS-WO_3, and CdS-Au-WO_3. The XRD pattern of WO_3-240 shows that the wall of macrospore is highly crystalline and all the Bragg peaks can be indexed to the monoclinic phase of WO_3 (JCPDS no. 43-1035), which is consistent with the SAED result. After loading Au particles, a diffraction peak appearing at 38.2° was observed in Au-WO_3, and it corresponds to Au (111) lattice face of fcc structure (JCPDS no. 04-0784). The typical diffraction peaks for CdS (JCPDS no. 65-2887) was found in CdS-WO_3 and CdS-Au-WO_3, confirming the formation of crystalline CdS after hydrothermal depositing. The peak of Au is also observed in CdS-Au-WO_3, which indicates the presence of WO_3, Au and CdS in the three-component system.

Fig.5b presents the UV-vis diffuse reflectance spectra of WO_3-240, Au-WO_3, CdS-Au-WO_3 PC segments (solid lines), and crushed WO_3 (dash line). For pure crushed WO_3, the strong absorption at wavelength range below 470 nm is due to the

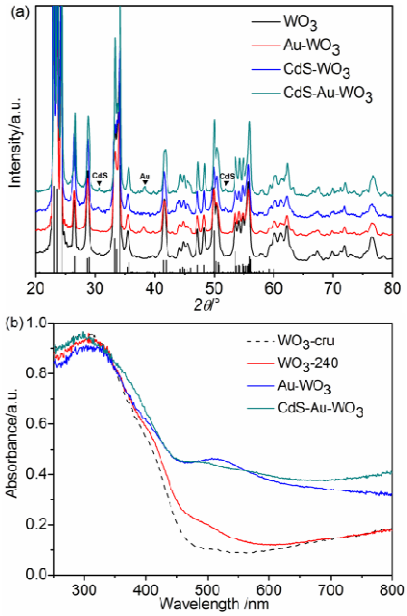

Fig.5 XRD patterns (a) of pure WO_3, Au-WO_3, CdS-WO_3 and CdS-Au-WO_3 composites. UV-vis diffuse reflectance absorption spectra (b) of WO_3-240, Au-WO_3, CdS-Au-WO_3 photonic crystal segments (solid lines), and crushed WO_3 (dash line).

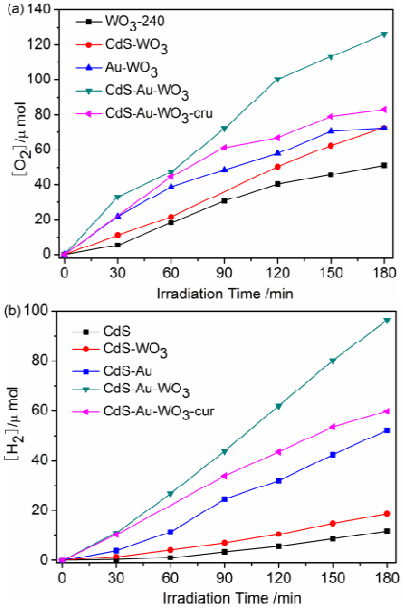

Fig.6 Photocatalytic oxygen evolution (a) from the WO_3-240, CdS-WO_3, Au-WO_3, CdS-Au-WO_3 and crushed CdS-Au-WO_3 photocatalysts in the presence of 5 mmol $AgNO_3$ as a hole donor, and photocatalytic hydrogen evolution (b) from pure CdS, CdS-WO_3, CdS-Au, CdS-Au-WO_3 and crushed CdS-Au-WO_3 photocatalysts in the presence of 20 mmol Na_2S and Na_2SO_3 as an electron donor.They are all illuminated under visible-light over 100 mL aqueous solution containing 20 mg photocatalysts. 300 W Xe arc lamp with a UV-cutoff filter (≥420 nm) used as the visible-light source.

intrinsic absorption of WO_3. The absorption enhancement of WO_3-240 in the region of below 400-600 nm is contributed to the location of the slow photons at the red-edge of thestopband[15] and multiple scattering among the segments. Compared with pure WO_3, Au-WO_3 composite shows a broad peak at 518 nm, which corresponding to plasmon resonance absorption (PRA) of Au nanoparticles. The peak position and shape of PRA indicate that the sizes of supported Au nanoparticles are smaller than 5 nm,[22] which is consistent with the TEM statistic result. After coating CdS, a small shoulder peak at 500 nm of CdS-Au-WO_3 appeared, which is attributed to the intrinsic absorption of CdS shell.[8a] The PRA peak of Au nanoparticles on CdS-Au-WO_3 shifted to 570 nm and broadened due to the strong electromagnetic coupling of Au and CdS.[23]

The photocatalytic activity of the samples were evaluated separately by monitoring oxygen and hydrogen evolution from visible light photocatalytic oxidation and reduction water in the presence of $AgNO_3$ as hole donors and Na_2S and Na_2SO_3 as electron donors, respectively. Control experiments indicated that no appreciable oxygen and hydrogen production were detected in the absence of either irradiation or photocatalyst, suggesting that hydrogen and oxygen were produced by photocatalytic reactions on the photocatalyst under irradiation. Fig.6a shows the time course of O_2 evolution of WO_3-240 PC segments, CdS-WO_3, Au-WO_3, CdS-Au-WO_3 and crushed CdS-Au-WO_3-cru samples. After depositing CdS and Au on the WO_3 PC segments, the photocatalytic activities of O_2 production on CdS-WO_3 (24.5μmol·h^{-1}/20 mg) and Au-WO_3 (27.7 μmol·h^{-1}/20 mg) were both improved. The photocatalytic activity is enhanced step-by-step from pure WO_3, Au-WO_3 to CdS-Au-WO_3 heterostructure. The CdS-Au-WO_3 3C system shows the best performance for photocatalytic O_2 evolution (45.4 μmol·h^{-1}/20 mg). These results show that the fabrication of CdS-Au-WO_3 heterostructure can effectively enhance the photocatalytic activity of WO_3 photonic crystal. The much more improved photocatalytic activity of CdS-Au-WO_3 than those of single- and two-component (2C) systems is ascribed to the strengthening of the interface charge carrier transfer between CdS and WO_3 (Scheme S1†). After introducing Au into the interface of WO_3 and CdS, vectorial electron transfer (WO_3→Au→CdS) driven by the two-step excitation of WO_3 and CdS was speculated as a main path, which effectively promotes the separation of photogenerated charge carriers.[8a]

Fig.6b shows plot of H_2 production from pure CdS, CdS-WO_3, CdS-Au, CdS-Au-WO_3 and crushed CdS-Au-WO_3-cru 3C system. All the samples exhibit photocatalytic activity for H_2 evolution. Among them, composite systems display higher activity than pure CdS. CdS-Au-WO_3 exhibit the highest activity (34.6 μmol·h^{-1}/20 mg), far exceeding those of the pure CdS (4.0 μmol·h^{-1}/20 mg) and 2C system CdS-WO_3 (6.3 μmol·h^{-1}/20 mg) and CdS-Au (16.5 μmol·h^{-1}/20 mg). These results suggest that the fabrication of CdS-Au-WO_3 heterostructure can effectively enhance the charge separation and H_2 evolution efficiency. The difference in the morphology of CdS (Fig.S7-8†) among the four samples might make the activity comparison difficult, however, the far higher activity of CdS-Au-WO_3 than others fully shows that the superiority of 3C heterostructure system. The excellent photocatalytic activities of CdS-Au-WO_3 for both H_2 and O_2 evolution confirm the efficient charge transfer among the whole 3C system. In addition, the structure stability and photostability of the as-prepared CdS-Au-WO_3 for H_2 evolution was also investigated.[25] The result shows that the sample possesses good structure stability and photostability with no obvious structure destruction and degradation of the activity during the continuous stirring and illumination for about 12 h and 64.5 h (Fig.S9-11†)

respectively.

To investigate the function of slow photon enhancement in the CdS-Au-WO_3 3C heterostructure system, CdS-Au-WO_3 was ground cruelly (denoted as CdS-Au-WO_3-cru). According to Fig. 6, CdS-Au-WO_3-cru shows lowered activity for both photocatalytic O_2 and H_2 evolution in varying degrees than uncrushed one. It is demonstrated that the slow photon enhancement plays an important role for improving photocatalytic activity in the 3C CdS-Au-WO_3 system. The slow photon enhancement on the activity of photocatalytic O_2 evolution could be easily understood, because that O_2 is mainly produced from the sub-component of WO_3 PC. Furthermore, the slow photon effect also works for improving H_2 evolution, even though the red edge of the stop-band of PC mismatches the absorption of CdS. It is supposed that the improvement of H_2 production is contributed to the recombination of electrons from slow photon enhancement of WO_3 with the holes in valence band of CdS via the bridge of Au, leading to an increase in the number of the electrons for excitation and to the lessened recombination of photogeneration carriers of CdS. Therefore, the superior performance of structural CdS-Au-WO_3 is resulted from the synergetic effect of efficient electron transfer of heterostructure and light harvesting of PC.

Conclusions

In summary, a visible-light responsive photonic crystal-based heterostructure CdS-Au-WO_3 was successfully fabricated by orderly depositing Au and CdS onto the framework of structured WO_3 inverse opal photonic crystal segments. It shows superior activity of photocatalytic water splitting both for hydrogen and oxygen evolution under visible light illumination. The excellent performance is attributed to the synergistic integration of good light harvesting of photonic crystals and efficient electron transfer of heterostructure. The construction of photonic crystal-based heterostructure system is expected to throw new light on the design of highly efficient photocatalyst for overall water splitting.

Acknowledgements

This work is supported by the National Science Foundation of China (Grant No. 20806092, U1162117), Beijing Nova Program (Grant No. Z11111005450000), Program for New Century Excellent Talents in University (NCET-11-0732), PetroChina Innovation Foundation (2011D-5006-0403), and Science Foundation of China University of Petroleum, Beijing (Nos. KYJJ2012-03-09, LLYJ-2011-59, QZDX-2011-02)

Notes and references

State Key Laboratory of Heavy Oil Processing,China University of Petroleum, Beijing 102249,China. Fax: (+86)10-6972-4721; E-mail: jianggy@cup.edu.cn, xcm@cup.edu.cn

#These authors contributed equally to this work

†Electronic Supplementary Information (ESI) available: [details of any supplementary information available should be included here]. See DOI: 10.1039/b000000x/

1 a) X. B. Chen, S. H. Shen, L. J. Guo, S. S. Mao, *Chem. Rev*. 2010, **110**, 6503.; b) A. Kudo, Y. Miseki, *Chem. Soc. Rev*. 2009, **38**, 253.

2 R. Asahi, T. Morikawa, T. Ohwaki, K. Aoki, Y. Taga, *Science* 2001,**293**, 269.

3 S. Linic, P. Christopher, D. B. Ingram, *Nat. Mater*. 2011, **10**,911.

4 a) A. Kubacka, M. Fernández-García, G. Colón, *Chem. Rev*. 2012, **112**, 1555; b) H. G. Yang, C. H. Sun, S. Z. Qiao, J. Zou, G. Liu, S. C. Smith, H. M. Cheng, G. Q. Lu, *Nature* 2008, **453**, 638.

5 a) H. J. Li,Y. Zhou, L. Chen, W. J. Luo, Q. F. Xu, X. Y. Wang, M. Xiao, and Z. G. Zou, *Nanoscale*, 2013, **5**, 11933; b) H. Kim, Y. Tak, K. Senthil, J. Joo, S. Jeon and K. Yong, J. Vac. Sci.Techno.B. 2009, **27**, 2182.

6 X. F. Cui, G. Y. Jiang, M. Zhu, Z. Zhao, L. C. Du,Y. X. Weng, C. M. Xu, D. K. Zhang, Q. L. Zhang, Y. C. Wei, A. J. Duan, J. Liu, J. S. Gao, *Int.J.Hydrogen Energy*, 2013, **38** 9065.

7 Y. J. Wang, R. Shi, J. Lin and Y. F. Zhu, *Energy Environ. Sci*. 2011, **4**, 2922.

8 a) H. Tada, T. Mitsui, T. Kiyonaga, T. Akita, K. Tanaka, *Nat. Mater*. 2006, **5**, 782; b) H. M. Zhu, B. F. Yang, J. Xu, Z. P. Fu, M. W. Wen, T. Guo, S. Q. Fu, J. Zuo, S. Y. Zhang, *Appl. Catal. B-Environ*. 2009, **90**, 463; c) H. J. Yun, H. Lee, N. D. Kim, D. M. Lee, S. Yu, J. Yi, *ACS Nano*, 2011, **5**, 4084; d) Z. B. Yu, Y. P. Xie, G. Liu, G. Q. Lu, X. L. Ma, H. M. Chen, *J. Mater. Chem*. A 2013, **1**, 2773; e) L. Ding, H. Zhou, S. A. Lou, J. Ding, D. Zhang, H. X. Zhu, T. X. Fan, *Int. J. Hydrogen Energy* 2013, **38**, 8244.

9 K. P. Xie, Q. Wu, Y. Y. Wang, W. X. Guo, M. Y. Wang, L. Sun, C. J. Lin, *Electrochem. Commun.* 2011, **13**, 1469.

10 a) A. Iwase, Y. H. Ng, Y. Ishiguro, A. Kudo, R. Amal, *J. Am. Chem. Soc*. 2011, **133**, 11054; b) Y. J. Wang, F. M. Wang and J. He, *Nanoscale*, 2013, **5**, 11291.

11 Y. Cao, J. O. Schenk, M. A. Fiddy, *Optics and Photonics Letters* 2008, **1**, 1.

12 P. Russell, *Science* 2003, **299**, 358.

13 M. F. Yanik, S. Fan, M. Soljačić, J. D. Joannopoulos, *Opt. Lett.* 2003, **28**, 2506.

14 a) J. I. L. Chen, G. Freymann, S. Y. Choi, V. Kitaev, G. A. Ozin. *Adv. Mater.* 2006, **18**, 1915; b) N. Nishimura, N. Abrams, B. A. Lewis, L. I. Halaoui, T. E. Mal-louk, K. D. Benk stein, J. Van de Lagemaat, A. J. Frank, *J. Am. Chem. Soc*. 2003, **125**, 6306.

15 X. Q. Chen, J. H. Ye, S. X. Ouyang, Te. Kako, Z. S. Li, Z. G. Zou, *ACS Nano* 2011, **5**, 4310.

16 J. Liu, G. L. Liu, M. Z. Li, W. Z. Shen, Z. Y. Liu, J. X. Wang, J. C. Zhao, L. Jiang, Y. L. Song, *Energy Environ. Sci*. 2010, **3**, 1503.

17 P. Jiang, K. S. Hwang, D. M. Mittleman, J. F. Bertone, V. L. Colvin, *J. Am. Chem. Soc*. 1999, **121**, 11630.

18 a) M. Sadakane, K. Sasaki, H. Kunioku, B. Ohtani, R. Abe, W. Ueda, *J. Mater. Chem*. 2010, **20**, 1811; b) M. Sadakane, K. Sasaki, H. Kunioku, B. Ohtani, W. Ueda, R. Abe, *Chem. Commun*. 2008, **48**, 6552.

19 J. X. Wang, Y. Q. Wen, H. L. Ge, Z. W. Sun, Y. M. Zheng, Y. L. Song, L. Jiang, *Macromol. Chem. Phys*. 2006, **207**, 596.

20 Y. C. Wei, J. Liu, Z. Zhao, A. J. Duan, G. Y. Jiang, C. M. Xu, J. S. Gao, H. He and X. P. Wang, *Energy Environ. Sci.* 2011, **4**, 2959

21 G. Q. Xu, B. Liu, S. J. Xu, C. H. Chew, S. J. Chua, L. M. Gana, *J. Phys. Chem. Solids* 2000, **61**, 829.

22 V. Subramanian, E. E. Wolf, P. V. Kamat, *J. Am. Chem. Soc*. 2004, **126**, 4943.

23 I. Honma, T. Sano, H. Komiyama, *J. Phys. Chem*. 1993, **97**, 6692.

24 a) M. Miyauchi , Y. Nukui , D. Atarashi , and E. Sakai *ACS Appl. Mater. Interfaces* 2013, **5**, 9770; b) X. W. Wang, G. Liu, Z. G. Chen, F. Li, L. Z. Wang, G. Q. Lu and H. M. Cheng, *Chem. Commun*. 2009, **23**, 3452.

25 F. Y. Song, Y. Ding, B. C. Ma, C. M Wang, Q. Wang, X. Q. Du, S. Fu and J. Song, *Energy Environ. Sci.* 2013, **6**, 1170.